GeV gamma-ray attenuation and the high-redshift UV background

Rudy C. Gilmore,[1]* Piero Madau,[2] Joel R. Primack,[1] Rachel S. Somerville[3]
and Francesco Haardt[4]

[1]*Department of Physics, University of California, Santa Cruz, CA 95064, USA*
[2]*Department of Astronomy & Astrophysics, University of California, Santa Cruz, CA 95064, USA*
[3]*Space Telescope Science Institute, 3700 San Martin Dr., Baltimore, MD 21218, USA*
[4]*Dipartimento di Fisica e Matematica, Universitá dell'Insubria, Via Valleggio 11, 22100 Como, Italy*

ABSTRACT

We present new calculations of the evolving UV background out to the epoch of cosmological reionization and make predictions for the amount of GeV gamma-ray attenuation by electron–positron pair production. Our results are based on recent semi-analytic models of galaxy formation, which provide predictions of the dust-extinguished UV radiation field due to starlight, and empirical estimates of the contribution due to quasars. We account for the reprocessing of ionizing photons by the intergalactic medium. We test whether our models can reproduce estimates of the ionizing background at high redshift from flux decrement analysis and proximity effect measurements from quasar spectra, and identify a range of models that can satisfy these constraints. Pair production against soft diffuse photons leads to a spectral cut-off feature for gamma rays observed between 10 and 100 GeV. This cut-off varies with redshift and the assumed star formation and quasar evolution models. We find only negligible amounts of absorption for gamma rays observed below 10 GeV for any emission redshift. With observations of high-redshift sources in sufficient numbers by the *Fermi Gamma-ray Space Telescope* and new ground-based instruments, it should be possible to constrain the extragalactic background light in the UV and optical portion of the spectrum.

Key words: intergalactic medium – gamma rays: bursts – cosmology: theory – gamma rays: theory – diffuse radiation – ultraviolet: galaxies.

1 INTRODUCTION

Interactions between photons via electron–positron pair production can have a substantial effect on the observed spectra of extragalactic gamma-ray sources. This process, which can occur when the required threshold energy of twice the electron mass is present in the centre-of-mass frame, removes gamma rays en route to the observer (Gould & Schreder 1967) and provides a link between high-energy astrophysics and the extragalactic background light (EBL) – the integrated luminosity of the universe at UV, optical and IR frequencies.

Attempts to measure the present-day EBL through absolute photometry in the optical and IR portion of the spectrum are hampered by the bright foregrounds of the Milky Way and zodiacal light from dust in the solar system, as well as calibration uncertainties (Hauser & Dwek 2001). Measurements in the near- and far-IR are available from the DIRBE and FIRAS experiments on the *COBE* satellite (Fixsen et al. 1998; Hauser et al. 1998; Lagache et al. 2000; Wright

& Reese 2000; Cambrésy et al. 2001; Wright 2001, 2004; Levenson, Wright & Johnson 2007). A tentative determination of the optical EBL was made in Bernstein, Freedman & Madore (2002a,b) with revision in Bernstein (2007). Number counts of observed galaxies provide a robust lower limit to the EBL, but the degree to which these measurements converge can be controversial. The analysis of the integrated galaxy counts in seven optical and near-IR bands by Madau & Pozzetti (2000) showed that flux from direct starlight converged to a fairly low level, below that claimed in the several DIRBE detections of near-IR flux. Recent experiments such as the *Galaxy Evolution Explorer* (*GALEX*) satellite, *Infrared Space Observatory* (*ISO*) and *Spitzer* have provided counts data in a variety of non-optical wavelengths, placing lower limits on the local EBL at most wavelengths of interest. A more thorough discussion of current EBL constraints can be found in Gilmore, Primack & Somerville (in preparation) and Primack, Gilmore & Somerville (2008).

A number of techniques have been employed to build cosmological models of the emission of light from galaxies at UV to far-IR wavelengths. These include interpolation and extrapolation of cosmological observables such as star formation rate (SFR) (Kneiske,

*E-mail: rgilmore@physics.ucsc.edu

Mannheim & Hartmann 2002; Kneiske et al. 2004; Razzaque, Dermer & Finke 2009) and luminosity functions (LFs) (Franceschini, Rodighiero & Vaccari 2008). Another method evolves backwards in time the local galaxy population, usually by assuming that the luminosity density changes with redshift as a power law at all wavelengths (Stecker, Malkan & Scully 2006). A third class of techniques models the galaxy population forward in time, beginning with cosmological initial conditions (Primack et al. 2001; Primack, Bullock & Somerville 2005).

Our goal in this paper is to build a suite of models of the evolving background light produced by stars and quasars, with a focus on the optical-UV background out to high redshift. A preliminary report on this work appeared in Gilmore et al. (2008). We calculate the reprocessing of ionizing radiation by the intergalactic medium (IGM) using the radiative transfer code CUBA (Haardt & Madau 1996), and use the observed ionization state of the IGM to constrain our models. The contribution of starlight to the EBL is predicted by recent semi-analytic models (SAMs) of galaxy formation, described in Somerville et al. (2008), hereafter S08. These have been used by Gilmore et al. (in preparation) (see also Primack et al. 2008) to make predictions for the evolving EBL. Most previous modelling attempts, including our recent work with this new SAM, have focused on observational data in the optical and IR. These are the wavelengths most relevant to observations of relatively nearby ($z < 0.5$) blazars with ground-based instruments, which until recently have typically featured energy thresholds above ~150 GeV. With the recent launch of *Fermi* with its Large Area Telescope (LAT) sensitivity range of 20 MeV to 300 GeV, as well as the advent of new ground-based experiments such as MAGIC-II with energy thresholds <100 GeV, it is now important to make theoretical predictions of the UV background at ionizing and non-ionizing wavelengths out to high redshift. This paper is an attempt to specifically target absorption in this region of the gamma-ray spectrum.

Understanding the absorption that occurs for gamma rays observed between 1 and 100 GeV is an uncertain undertaking due to the lack of sensitive observations of the EBL at the corresponding UV wavelengths. Moreover, the declining opacities for gamma rays in this region means that sources are likely to be visible out to large redshift. Evolution of the background must be taken into account when calculating absorption for all but the nearest blazars, and at high redshifts the EBL can have a spectral energy distribution (SED) much different than observed locally. The most distant object with confirmed redshift that has been detected at VHE energies is currently the flat-spectrum radio quasar (FSRQ) 3C 279 (Albert et al. 2008) at $z = 0.536$. This object was observed at energies between 90 and 500 GeV, with a steep spectrum that was likely due in part to EBL absorption. In the 10 to 100 GeV energy decade that is now being probed by *Fermi* and upgraded ground experiments, the characteristic redshift at which the EBL becomes optically thick to pair production is expected to increase to redshifts of several.

A small number of calculations have been performed that specifically addressed the question of the gamma-ray absorption by the UV background. In Madau & Phinney (1996), two different models of star formation, based on different assumptions about the *B*-band normalization, were used to predict gamma-ray opacities from 10 to 200 GeV, with propagation of ionizing photons through the IGM taken into account. This work suggested that the universe becomes optically thick at a few tens of GeV for gamma rays emitted at $z \sim$ 2. A second work which focused on the UV background (Oh 2001) argued that the absorption by ionizing photons was negligible, and that <20 GeV observed gamma rays would only be significantly attenuated at higher redshifts, where they would interact with photons

below the Lyman limit. Lyα photons were found to be a significant component of the UV flux. This paper also explored the possibility of using *Fermi* to detect an evolving blazar attenuation edge, which would probe high-redshift star formation. Finally, the background model of Salamon & Stecker (1998) targeted absorption of 10–500 GeV gamma rays, and used an estimate of high-redshift star formation based on evolution seen in damped Lyα systems. This work also included a UV contribution from quasars.

At energies below the Lyman limit, lower bounds on galaxy emissivity exist from number counts by *GALEX* (Xu et al. 2005) and *Hubble Space Telescope* (*HST*), as well as balloon-based experiments (Gardner, Brown & Ferguson 2000). Such experiments are subject to systematic errors in completeness and photometric measurement of apparent magnitude, and can only test the background out to moderate redshift. At higher redshifts, we no longer have measurements that directly connect to the EBL, such as direct number counts and absolute photometry, and uncertainties and possible biases in cosmological measurements such as LFs and star formation rate density (SFRD) become increasingly problematic.

Measurements of the ionization state of the IGM can provide constraints on ionizing flux. At redshifts higher than the 'breakthrough redshift' ≈ 1.6, the universe is optically thick to Lyman continuum photons, and ionizing fields become local, with a mean free path that decreases rapidly at larger redshifts (Madau, Haardt & Rees 1999), while below this redshift the mean free path becomes longer than the horizon length. Studies of the opacity of Lyα and other redshifted absorption lines place constraints on the emission of UV photons by probing the neutral fraction, and therefore the balance between photoionizations and recombinations (Haehnelt et al. 2001; Madau et al. 2004). As these lines are affected by the local radiation, they provide information about sources existing at approximately the redshift of the absorber (Haardt & Madau 1996).

Two methods of determining the ionization state of the IGM include the proximity effect, in which one searches for the decrease in Lyα emissions near an active galactic nuclei (AGN) (Liske & Williger 2001; Dall'Aglio, Wisotzki & Worseck 2008), and flux decrement analysis, which utilizes hydrodynamic simulations to model the distribution of Lyα absorption along the line of sight to an AGN (e.g. Bolton et al. 2005). The line-of-sight proximity effect utilizes the decrease in absorption lines in the vicinity of a quasar, compared to farther away along the line of sight, due to increased ionization fraction. As the quasar has a known UV luminosity, the deficit of absorption in this region can be used to estimate the background; a larger change indicates a lower background flux. As quasars do not reside in typical cosmological environments, a number of potential biases exist. Quasars tend to be found in overdense environments, which can lead to overestimates of the background flux by as much as a factor of 3 (Loeb & Eisenstein 1995). Time variation in luminosity on the time-scale of photoionization, typically $\sim 10^4$ years, will also tend to bias results towards a high background, as quasars tend to be selected in their brightest phases (Schirber, Miralda-Escudé & McDonald 2004). It is also now recognized that using broad emission lines such as Lyα tends to lead to underestimated redshifts and, therefore, higher quasar luminosity (Richards et al. 2002). This may have been a problem in many determinations of the proximity effect. The assumed cosmological model also affects the resulting background inferred by these measurements. The second method mentioned, the less-direct flux decrement technique (Rauch et al. 1997), is not without its own potential biases; it relies on correct cosmological parameters and knowledge of the quasar's unabsorbed continuum level, a

problem at high redshift where absorption is strong. Newer attempts to correct for the biases in proximity effects measurements, such as Dall'Aglio et al. (2008), have found lower values for the ionizing background flux that are more consistent with the flux decrement technique.

Observations of the Lyα forest can also provide clues about the types of sources producing the ionizing background, which in our model include star-forming galaxies and quasars. The quasar LF has been measured by large-scale surveys such as the Two-degree Field (2dF) (Boyle et al. 2000) and the Sloan Digital Sky Survey (SDSS) (Croom et al. 2004; Jiang et al. 2006; Richards et al. 2006), and data are also available at a variety of frequencies from experiments such as *XMM*, *Chandra* and *Spitzer* (Barger et al. 2005; Matute et al. 2006). The hydrogen of the IGM is known to be fully ionized below a redshift of ∼6 (Fan et al. 2006). Photons above the Lyman limit are responsible for reionizing the universe and maintaining it in a highly ionized state. The relative contributions of star-forming galaxies and AGN to this process are not fully understood, but there is evidence that quasars are a sub-dominant component at this epoch. The decline of the quasar LF observed beyond redshift 3 constrains the quasar contribution to the ionizing background to be $\sim 10^{-2}$ (Fan et al. 2001; Madau et al. 1999), unless there is an unexpected steep upturn in the quasar LF at low luminosities. A new approach by Srbinovsky & Wyithe (2007) utilizing semi-analytic modelling sets limits on the quasar contribution to ionizing radiation of 1.4 to 14.5 per cent at $z = 5.7$, and studies of the soft X-ray background also constrain this fraction to be subdominant (Dijkstra, Haiman & Loeb 2004).

Increased quasar emission is believed to be responsible for He II reionization, which as tracked by He II Lyα absorption takes place at a lower redshift than hydrogen, $z \sim 3$ (e.g. Bolton et al. 2005). The shape of the ionizing background, therefore, evolves in redshift, with a hardening of the spectrum that is indicative of an increased contribution from quasars. The degree to which AGN dominate the UV background at the time of He reionization is a debated issue, with some suggestions that stars and AGN provide roughly equal contributions to the background at $z \sim 3$ (Kriss et al. 2001; Smette et al. 2002). One of the major sources of uncertainty in this transition lies in the unresolvable faint end of the AGN LF (Schirber & Bullock 2003, SB03). The ratio between hydrogen and helium ionization fractions, particularly H I (13.6 eV) and He II (54.4 eV), can be used to measure the slope of the total UV spectrum in this regime. The decrease in the optical depth of He II indicates that the harder radiation from quasars increases with time between $z = 5$ and 3 (Shull et al. 2004; Fan et al. 2006).

Aside from quasars, the known dominant sources of UV radiation are short-lived massive stars, mainly of O- and B-type, which closely trace the SFRD. Estimating the ionizing contribution from star-forming galaxies directly is complicated by the fact that only a small fraction f_{esc} of this radiation escapes from galaxies due to neutral gas and dust in the interstellar medium, as we will discuss in Section 2.4.

Because of the uncertain nature and evolution of sources of ionizing radiation, in this paper, we consider four models that attempt to span a realistic range of assumptions. In Section 2, we discuss the inputs to our model, including a short description of our SAMs, assumed quasar luminosity density and radiative transfer code. In Section 3, we introduce our four UV background models and present results, including the evolving background radiation and comparisons with Lyα forest measurements. The main results of the paper, gamma-ray opacities, are presented in Section 4, with a discussion following in Section 5. Our four models are summarized in

Table 1. The background models considered in this work. The second and third columns show the star formation histories and quasar luminosity densities used as inputs in each model. The escape fraction in the last column refers to the values used in calculating the background flux and optical depth to gamma rays in Figs 10 and 11, respectively. Our SFH scenarios are discussed at the beginning of this section. 'HRH07' refers to the best-fitting model of Hopkins et al. (2007), and 'SB03 model C' to the model in Schirber & Bullock (2003). We have multiplied the latter by a factor of 0.8 to better match the observed quasar luminosity density at low redshift. The escape fraction refers to the attenuation of ionizing photons from star-forming galaxies by neutral hydrogen; attenuation by dust is included intrinsically in our SAM.

Model	SFR density	Quasar luminosity	$f_{esc,HI}$
1	Fiducial	HRH07	0.1
2	Low	HRH07	0.2
3	Fid. High-peaked	HRH07	0.1
4	Fiducial	SB03 model C	0.02

Table 1, and their successes and failures in accounting for the data are summarized in Table 2.

2 MODELLING

To calculate the evolving UV background, we have used predictions of the UV luminosity density from galaxies, as provided by recent SAMs of galaxy formation, combined with estimates of quasar emissivity. The combined emissivities from galaxies and quasars are integrated over redshift to find the evolving background flux. Photons from these sources at energies above the Lyman limit can be absorbed and reradiated by the IGM; we calculate the effect of these processes using the CUBA radiative transfer code. In this section, we discuss the SAMs and radiative transfer code used in calculating the background, and show some general results.

2.1 The semi-analytic models

The SAMs used in calculating the EBL in this work are described in detail in S08, and are based on the models described in Somerville & Primack (1999) and Somerville, Primack & Faber (2001), with several new updates and capabilities; we provide a very brief summary in the following paragraphs. Interested readers should also see Primack et al. (2008) and Gilmore et al. (in preparation), which focused on the optical and IR EBL resulting from galaxies in this model.

The backbone of the SAMs are dark matter 'merger trees', which describe the cosmological assembly history of dark matter haloes as they build up over time through mergers and accretion of diffuse material. These merger trees may either be constructed via Monte Carlo techniques based on the Extended Press–Schechter theory (as in this work), or extracted from *N*-body simulations. We compute the rate at which gas can cool via atomic processes and be accreted onto the central galaxy within the potential well of each of these collapsed and virialized DM haloes. Cold gas is then converted into stars in both a 'quiescent' and starburst modes. The 'quiescent' mode takes place in isolated discs and is modelled according to an empirical prescription based on the Schmidt-Kennicutt law (Kennicutt et al. 1998). The starburst mode is triggered during mergers, with gas being rapidly converted into stars on time-scales determined from hydrodynamic simulations of galaxy mergers. Feedback from supernovae and massive stars can reheat cold gas and expel it from the galaxy. Chemical evolution is modelled using a simple

instantaneous recycling approximation with the effective yield treated as a free parameter.

The most recent models also treat the growth of supermassive black holes within galactic nuclei and the impact of the released energy on galaxies and their environment. Seed black holes, perhaps originating from the remnants of the very massive Population III stars, are planted in the top-level haloes in the merger trees, and can grow by two accretion mechanisms. Galaxy mergers trigger rapid (Eddington limited) 'bright mode' accretion and correspond observationally to classical X-ray or optically luminous quasars and AGN. Bright mode AGN activity drives winds that can expel cold gas from the galaxy. Accretion of hot gas from the hot halo feeds low-level (Bondi) 'radio mode' accretion, which is associated with the production of giant radio jets. These jets are assumed to be capable of heating the surrounding hot gas halo, offsetting or even quenching cooling flows. Although the radio mode feedback in particular has been shown to play a key role in reproducing important galaxy properties in these models, such as galaxy colour bimodality and LFs, the predictions for observable properties of quasars and AGN in these models has not yet been thoroughly tested. Therefore, in this work, we instead add in the contribution to the background radiation due to quasars empirically.

The star formation and chemical enrichment histories for each galaxy are convolved with stellar population models to produce synthetic SEDs. We make use of the Bruzual & Charlot (2003) models with a Chabrier stellar initial mass function (IMF).

Our models include a simple estimate of the attenuation of starlight due to dust, based on a two-component model similar to that proposed by Charlot & Fall (2000). One component is the diffuse 'cirrus' dust in the disc and another is associated with the dense 'birth clouds' surrounding young star-forming regions. The V-band, face-on extinction optical depth of the diffuse dust is given by

$$\tau_{V,0} \propto \frac{\tau_{\rm dust,0}\, Z_{\rm cold}\, m_{\rm cold}}{(r_{\rm gas})^2}, \tag{1}$$

where $\tau_{\rm dust,0}$ is a free parameter, $Z_{\rm cold}$ is the metallicity of the cold gas, $m_{\rm cold}$ is the mass of the cold gas in the disc and $r_{\rm gas}$ is the radius of the cold gas disc. To compute the actual extinction, we assign each galaxy a random inclination and use a standard 'slab' model. Additionally, stars younger than 10^7 yr are enshrouded in a cloud of dust with optical depth $\tau_{\rm BC,V} = \mu_{\rm BC}\, \tau_{V,0}$, where $\mu_{\rm BC} = 3$. Finally, to extend the extinction correction to other wavebands, we assume a Galactic attenuation curve (Cardelli, Clayton & Mathis 1989) for the diffuse dust component and a power-law extinction curve $A_\lambda \propto (\lambda/5500\,\text{Å})^n$, with $n = 0.7$, for the birth clouds. The free parameters are adjusted to reproduce the observed ratios of far-UV to far-IR luminosity in nearby galaxies.

We consider two different choices of parameters for our SAMs, which differ primarily in the assumed cosmological parameters. The free parameters that control galaxy formation in each model are then tuned to match local galaxy observations, as described in S08 (the actual values of the parameters for both models are also given in S08, Table 2). The 'fiducial' model adopts a concordance cosmology with $\Omega_m = 0.3$, $\Omega_\Lambda = 0.7$, $h = 0.70$ and $\sigma_8 = 0.90$. Our 'low' model adopts the best-fitting values from *Wilkinson Microwave Anisotropy Probe* 3 (*WMAP*3) for these parameters, with $\Omega_m = 0.2383$, $\Omega_\Lambda = 0.7617$, $h = 0.732$ and $\sigma_8 = 0.761$. The most relevant difference in this work is the value of the power spectrum normalization σ_8. The lower normalization of the primordial power spectrum in the 'low' model leads to delayed structure formation and decreased luminosity densities at high redshifts (see S08). Adopting the best-
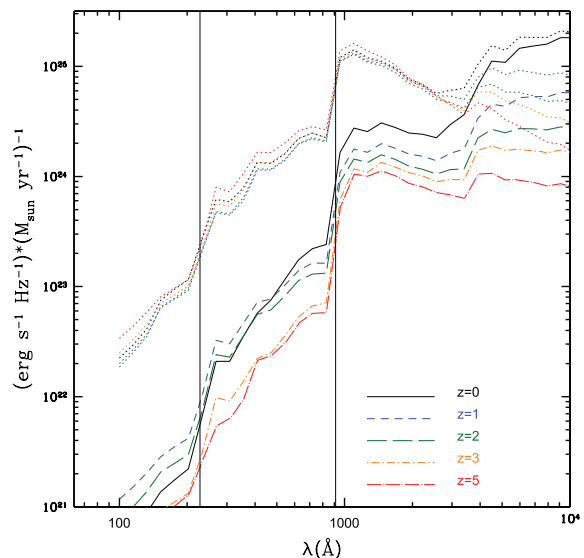

Figure 1. The emissivity due to galaxies predicted by our fiducial galaxy formation model at a number of redshifts, normalized to $1\,\text{M}_\odot\,\text{yr}^{-1}$. Dotted curves show the emission predicted in the absence of dust extinction. Vertical lines indicate the ionization energies of H I and He II at 912 and 228 Å.

fitting parameters from the more recent analysis of *WMAP*5, which favoured $\sigma_8 = 0.82$ (Komatsu et al. 2009), gives nearly identical results to our *WMAP*3 (low) models.

The predictions for attenuated and unattenuated emissivity from our fiducial SAM are shown for several redshifts in Fig. 1. Predictions from the 'low' model are qualitatively similar, although because of the delayed star formation, galaxies tend to have higher gas surface densities, and therefore higher dust opacities and larger attenuation values are predicted.

In our companion EBL paper (Gilmore et al. in preparation, see also Primack et al. 2008), we compare the predictions of our SAMs with a broad range of data, including local LFs, optical and IR luminosity density, and number counts in a variety of bands from the UV to far-IR. In a planned future paper, we will make a careful comparison of these models with the galaxy population at high redshift. Here, we show just a few representative results demonstrating that our models are doing reasonably well at reproducing the UV properties of local and distant galaxies. In Fig. 2, we compare our model predictions with galaxy number counts in two UV bands, using data from the *GALEX* satellite and other experiments. This provides a test of the low-redshift normalization of our model in the UV range. *GALEX* has surveyed the sky these bands and provided data down to magnitude ~ 23.5 (Xu et al. 2005). At fainter magnitudes, there are measurements from the STIS instrument on the *HST* (Gardner et al. 2000), albeit with large uncertainty due to poor statistics. Populations of brighter objects have also been probed by the FOCA balloon-borne UV telescope, and counts from this instrument at 2000 Å have typically yielded higher numbers than *GALEX* after wavelength correction, possibly due to differences in calibration. Our models show good agreement with the data at 2310 Å, but are a bit higher than the *GALEX* observations at 1530 Å, though they are not in disagreement with the FOCA data.

Recent data from a variety of instruments has constrained the UV luminosity density out to high redshift. In Fig. 3, we have compared the UV emissivity in galaxies from our models against data at a rest-frame emission wavelength of approximately 1500 Å. We find that data from the *GALEX*-VVDS, GOODS and deep *HST* ACS
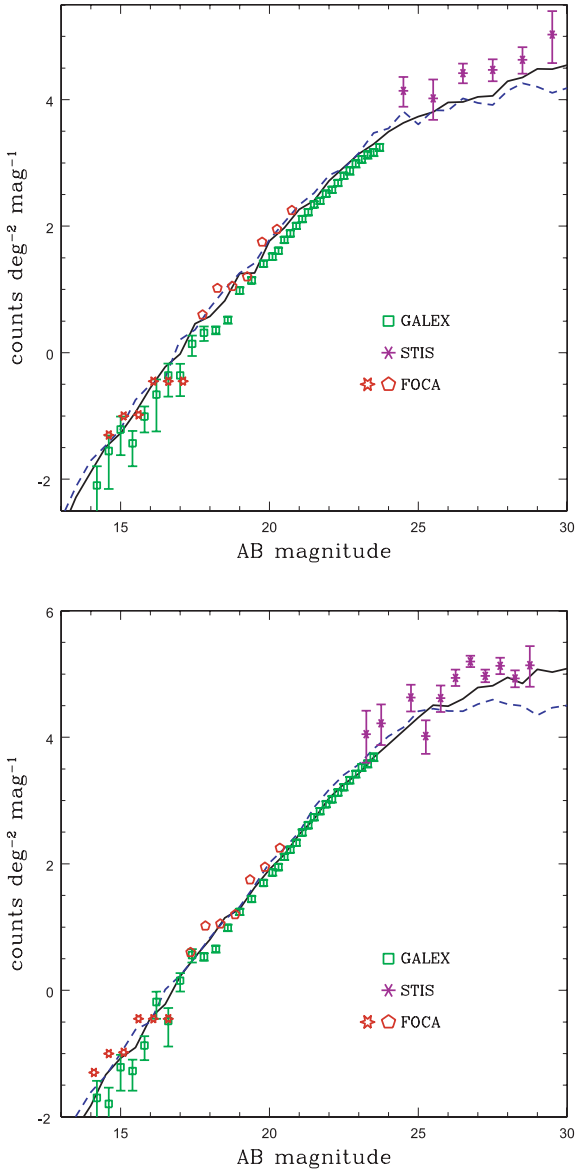
Figure 2. Number counts in the *GALEX* 1530 Å (upper) and 2310 Å bands (lower). The solid black line shows the fiducial model, and dashed blue shows the low model. Note that the low model has counts equal to or slightly greater than the fiducial model at some magnitudes; this is due to differing amounts of dust extinction at low redshift between the two models. Data are from *GALEX* (Xu et al. 2005, green squares), STIS on *HST* (Gardner et al. 2000, purple asterisks) and the balloon-borne FOCA experiment (Iglesias-Páramo et al. 2004; Milliard et al. 1992, red stars and open pentagons, respectively). Following Xu et al. (2005), all counts have been converted to the *GALEX* bands by assuming a UV spectral slope of −0.8.

imaging all agree reasonably well with the UV evolution of our fiducial model.

2.2 Star formation

The SFRD as a function of redshift in the 'fiducial' and 'low' models are shown in Fig. 4, compared with observational estimates of star formation density at various redshifts, all of which has been converted to a Chabrier IMF. At $z < 1$, both of our models are in good agreement with the observational compilation of Hopkins (2004), while at $1 < z < 2$ they tend to skirt the lower envelope
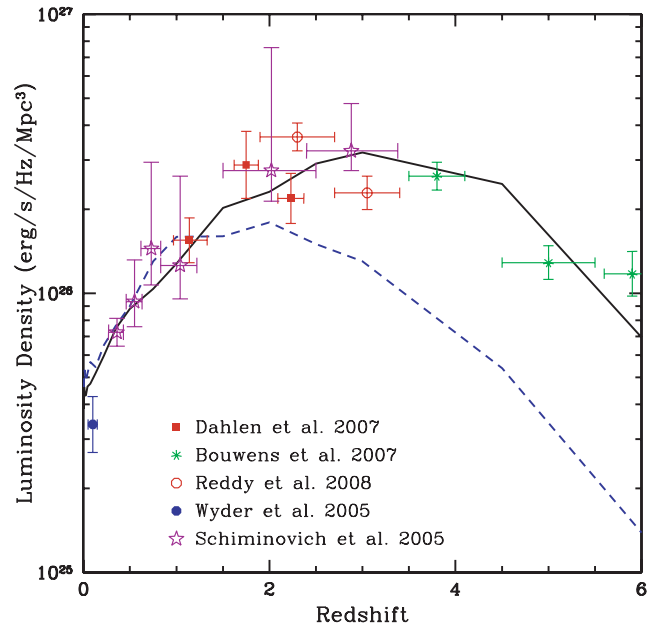

Figure 3. The emissivity at 1500 Å as a function of redshift in our models. As previously, the solid black line is the fiducial model, and the dashed blue line shows the low model. The blue circle at redshift 0.1 is GALEX data from Wyder et al. (2005) and the purple stars are measurements using GALEX and other data (Schminovich et al. 2005). The red squares are from GOODS (Dahlen et al. 2007), the red circles are determinations from ground-based observations (Reddy et al. 2008) and the green stars are from Bouwens et al. (2007).

of observational values. However, there are still large discrepancies between SFR estimates from different indicators and different data sets at these redshifts, in part due to the increased fraction of star formation in heavily obscured systems (e.g. Hopkins 2007), where the correction for dust obscuration is uncertain. At $z > 2$, the SFRD in the 'low' model declines fairly steeply, while in the fiducial model the SFRD remains nearly constant from $2 < z < 5$ and then declines more gradually. As discussed above and in S08, this is because of the lower normalization of the power spectrum and reduced small-scale power in this model, which delays the formation of structure.

Above redshift four, observational estimates of global SFRs diverge, and different measurements can disagree by as much as an order of magnitude. Studies of UV LFs of dropout galaxies by Bouwens and collaborators (Bouwens et al. 2008, 2007) find relatively low values for the global SFR, with a monotonic decrease above redshift four. Higher rates have been found by other authors, including those who have derived star formation history (SFH) from detections of gamma-ray bursts (GRBs) (Yüksel et al. 2008). These studies suggest a much higher rate of star formation which does not decrease significantly until $z > 6$. This may be due in part to the fact that the Bouwens et al. data points that we report here were obtained by integrating the UV LF down to a luminosity corresponding to 0.04 times the observed value of L_* at redshift 3. Other authors make different choices for the lower limit of integration, and the relatively steep slope of the UV LF at these redshifts implies that this can make a significant difference. The SAM predictions shown include the star formation in all galaxies (down to the mass resolution of the simulation).

Our 'low' SAM, based on the lower determination of σ_8 in *WMAP*3, produces a SFR that is lower than most of the data points at mid and high redshift, and reproduces the rapid fall-off in star
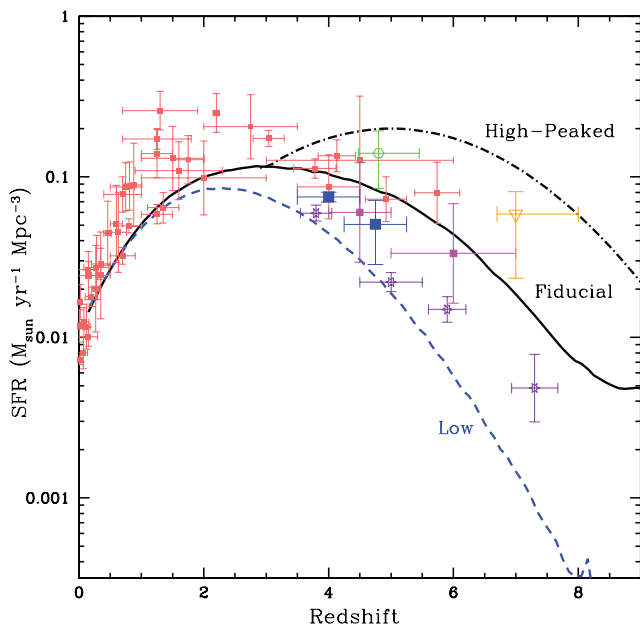
Figure 4. The global SFR density predicted by our models, compared with a compilation of observational data. The solid black and dashed blue curves show the SFRD history of our fiducial and low models, respectively. The black dash–dot curve which diverges from the fiducial curve above redshift 3 is the 'high-peaked' form which we discuss in the text. The red squares at lower redshift are from the compilation of Hopkins (2004). The purple stars are from observations of Bouwens et al. (2008, 2007) of dropout-selected galaxies. For these, we show the dust-corrected results from integrating the LFs down to a value of 0.04 L_* at $z = 3$; it is possible that fainter objects provide an additional contribution. The magenta squares at redshift 4.5 and 6 show inferred SFRs from GRB observations (Yüksel et al. 2008). The green circle is based on observations of Lyman-break galaxies at $z \sim 5$ (Verma et al. 2007), and the orange triangle is an upper limit from VLT data (Mannucci et al. 2007). The blue squares are results from the Subaru Deep Field (Ouchi et al. 2004). All data have been corrected for extinction (by the authors) and converted to a Chabrier IMF.

formation indicated by the Bouwens points. Our 'fiducial' model, based on *WMAP*1, does a better job of matching the higher SFRs seen in other dropout analyses, as well as the data from gamma-ray bursts.

Although not shown here, another way to constrain the SFH of the Universe is via the build-up of stellar mass in the form of long-lived stars. As shown in S08, the fiducial model predicts a stellar mass density that is higher than observational estimates by a factor of two at $z = 1$ and a factor of 3 at $z = 2$, while the 'low' (*WMAP*3) model produces good agreement with the stellar mass assembly history. As discussed in S08, this discrepancy between the observed stellar mass assembly history and the SFH has been pointed out in a number of recent papers (e.g. Fardal et al. 2007; Davé 2008), and one possible explanation is that the stellar IMF was more top-heavy in the past (so that more UV photons were produced per total unit mass of star formation). However, it is also still possible that the discrepancy is simply due to observational uncertainties in the estimates of SFRs and/or stellar masses.

In addition to the SFHs predicted self-consistently in our fiducial and low SAMs, we consider an additional ad hoc high-peaked fiducial form for the SFH above $z = 3$. This is not a SAM; it is simply a functional form that was chosen to be consistent with the highest observational determinations of the SFR. We then utilize the same redshift-dependent dust extinction factors as the fiducial

model. We include this case to illustrate the predictions for gamma-ray attenuation for an extreme model with the maximum plausible UV background at high redshift. However, we note that as the fiducial model already produces an integrated stellar mass density in excess of that observed at high redshift, the high-peaked model is strongly disfavoured by these observations.

2.3 Radiative transfer

Ionizing photons from galaxies and quasars which escape into the IGM are processed by neutral hydrogen and neutral and singly ionized helium which resides in Lyα forest clouds (LAC) and thicker Lyman-limit systems (LLS), defined here as having column densities $>10^{17.2}$ cm^{-2} . This has a strong effect on the spectrum and intensity of the average background field. The propagation of ionizing flux through the IGM in our models is calculated using an updated version of the CUBA code. An earlier version of CUBA is described in Haardt & Madau (2001) and is based on the theory of Haardt & Madau (1996). Here, we briefly summarize some of the main ideas and formalism from these papers.

The effect of residual neutral gas on the ionizing radiation field can be described in general terms by the radiative transfer equation:

$$\left(\frac{\partial}{\partial t} - \nu \frac{\dot{a}}{a} \frac{\partial}{\partial \nu} \right) J = -3\frac{\dot{a}}{a} J - c\kappa J + \frac{c}{4\pi}\epsilon. \tag{2}$$

Here, $J(\nu)$ is the intensity of the radiation field for frequency ν, $\epsilon(\nu)$ is the emissivity, a is the cosmological scale factor, c is the speed of light and κ is the continuum absorption coefficient. This equation accounts for both the redshifting of photons to lower energies, and absorption by neutral gas. Quasars and star-forming galaxies contribute to $\epsilon(\nu)$ in our model, along with the diffuse re-emission of absorption systems. Lyman absorbers are taken to have a distribution that can be described in terms of power laws in column density and redshift:

$$\frac{\partial^2 N}{\partial N_{\rm HI}\partial z} \propto N_{\rm HI}^{-1.5}(1 + z)^{\gamma} \tag{3}$$

with parameters

$\gamma = 0.16(\text{LAC}, 0 < z < 1.4),$

$\gamma = 3.0(\text{LAC}, 1.4 < z),$

$\gamma = 1.5(\text{LLS, all redshifts})$

used in these models. A distribution with slope -1.5 in column density has been shown to describe absorbers over a wide range in $N_{\rm HI}$ (Hu et al. 1995), and the slopes for redshift evolution are based on observational determinations (Bechtold 1994; Stengler-Larrea et al. 1995; Kim et al. 1997). The effective optical depth from the Lyα forest absorption in this distribution is shown in Fig. 5. Note that our Lyα optical depth does not follow the upturn seen at $z \sim 6$, where a rapid rise in absorption may signal that our assumption of a uniform UV background is no longer valid.

It should be noted that the exact form of the column distribution function is not critical, as it is the integrated value of this parameter from which we derive the effective optical depth and, therefore, the average background. The effective depth is dominated by clouds with opacity near unity. Using a power-law form simplifies the integration process, and speeds up our computation with little loss in accuracy. We do caution readers that the choice of distribution function can have a large effect on He II absorption, and in turn on the background above 54.4 eV which we report in Fig. 10. The
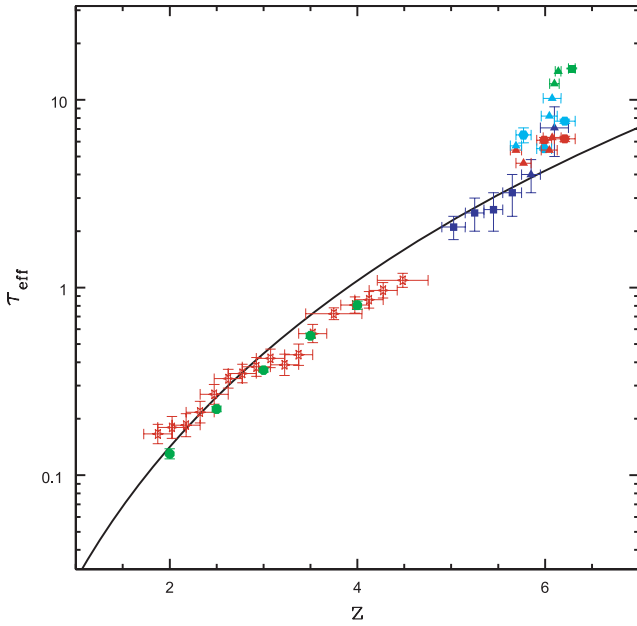
Figure 5. Effective optical depth as a function of redshift from our assumed absorption cloud distribution. Data from quasar spectra are shown at ($5 < z < 6.5$) from Fan et al. (2006); here the blue points are averaged Gunn–Peterson measurements, and the red, cyan and green symbols are Lyα, β and γ measurements of the highest redshift individual objects. Values at lower redshifts are from Schaye et al. (2003) (green circles) and Dall'Aglio et al. (2008) (red stars).

background at these energies is not expected to affect our gamma-ray attenuation significantly because the photon density at these high energies is so low.

Lyman systems reradiate a fraction of the absorbed light via recombination radiation. Our code accounts for the contribution of H I recombinations to the UV flux via free-bound, Lyα and two-photon continuum emission. For the latter two, only the non-ionizing background is affected. The total proper volume emissivity from IGM clouds from radiation released for a particular mode can be quantified as

$$\epsilon(\nu, z) = h\nu f_i(\nu) W_{\mathrm{abs}}(z) \Xi(z, \nu) \frac{\alpha_i}{\alpha_{\mathrm{tot}}} \frac{\mathrm{d}z}{\mathrm{d}l}, \qquad (4)$$

where α_i is the fraction of recombinations leading to the particular mode, which has probability $f_i(\nu)$ of creating a photon of energy ν. In the case of Lyman-α emission, this is simply a delta function at the line energy, and for the continuum distributions, descriptions can be found in Osterbrock (1989). The remaining functions contain the details of emission and absorption from absorption systems:

$$W_{\mathrm{abs}}(z) = \int_{\nu_{\mathrm{th}}}^{\infty} \frac{4\pi J(\nu', z)}{h\nu'} w_{\mathrm{abs}}(\nu') \, \mathrm{d}\nu' \qquad (5)$$

$$\Xi(z, \nu) = \int_0^{\infty} \frac{\partial^2 N}{\partial N_{\mathrm{H\,I}} \partial z} p_{em}(\nu, N_{\mathrm{H\,I}}) \, \mathrm{d}N_{\mathrm{H\,I}}. \qquad (6)$$

The first of these quantities is the rate of ionizations by the background field $J(\nu', z)$. Here, $w_{\mathrm{abs}}(\nu')$ encodes the information about the optical depth for photons of a given energy, and thus the probability of being absorbed. Equation (6) is the integral over absorption systems, multiplied by $p_{em}(\nu, N_{\mathrm{H\,I}})$, which is the probability of a photon of given energy escaping from a cloud after emission. The code does not include the contribution from sawtooth modulation due to H I and He II Lyman resonances (Madau & Haardt 2009).

We do not include radiation from recombinations to He I, as neutral helium is small in number density compared to both H I and He II (though that may not be the case at redshifts on the verge of reionization). As shown in Haardt & Madau (1996), thermal collisional effects can provide a sizable fraction (20 to 30 per cent) of the H I emission by Lyα and two-photon processes; these are not accounted for in our code. Collisions between He II atoms are never significant, as there is insufficient thermal energy to excite these modes.

2.4 Ionizing escape fraction from galaxies

The fraction of ionizing photons produced that escape from galaxies into the IGM is a free parameter in our model. This parameter is poorly constrained, with observations and simulations giving widely different and sometimes conflicting results. In the literature, the escape fraction may be defined in a couple ways. The absolute escape fraction is simply the fraction of radiation at wavelengths just shortwards of 912 Å which escapes the dust and neutral hydrogen in a galaxy. This definition is most relevant for the purposes of modelling the ionizing background. What is actually measured in observations is the relative escape fraction, where the ionizing flux is compared to a non-ionizing wavelength, often 1500 Å. As described below, we use a relative definition which separates the amounts of attenuation due to dust and H I (equation 7). Ionizing radiation from quasars is not attenuated in escaping the host galaxy in our model.

Direct detection of escaping UV radiation has only been successful in a handful of individual cases. As two of these detections have been for galaxies at $z \sim 3$ with large escape fractions measured (Shapley et al. 2006), the fact that many low-redshift attempts to find ionizing radiation have failed with low upper bounds may suggest evolution in this quantity between redshifts one and three. Rather firm upper limits on escape fraction from direct detection efforts exist for lower redshift galaxies (see the compilation in Siana et al. 2007). Steidel, Pettini & Adelberger (2001) reported ionizing flux from 29 stacked galaxies at $z \sim 3.4$, at a level indicating little or no attenuation. However, this result suffered from a selection bias, as the Lyman-break galaxies used were chosen from the bluest quartile of the population.

While observations have mainly determined upper limits on the ionizing escape fractions, some authors have used the ionization state of the IGM to derive lower limits. Ionization rates inferred from Lyα forest data and reasonable extrapolations of source number to faint luminosity can require a high escape fraction. Values of $\gtrsim$20 per cent above redshift 5 were found to be needed in Bolton & Haehnelt (2007). Srbinovsky & Wyithe (2008) have found that constraints on the escape fraction from $5.5 < z < 6.0$ from N-body simulations require a global minimum of 5 per cent to match Lyα data, with a higher fraction needed in the event that star formation in galaxies in smaller haloes is suppressed.

Recently, detailed adaptive mesh refinement (AMR) N-body hydrodynamical simulations of high-redshift galaxies ($3 < z < 9$) by Gnedin, Kravtsov & Chen (2008) have found low escape fractions of 1–3 per cent, without strong evolution in redshift or dependence on galaxy properties. This work found that most escaping ionizing radiation originated from stars in a thin shell at the outside of the H I disc. Smaller galaxies have less escaping radiation due to the fact that their H I discs are thicker relative to the distribution of young stars. Dust is found to have little effect on the escape of Lyman-continuum radiation, as the unobscured minority of stars that provide most of the escaping ionizing radiation

have essentially no attenuation due to dust, while stars that have translucent ($\tau \sim 1$) optical depths due to dust are generally completely obscured by H I. Another analysis has been undertaken using a smoothed particle hydrodynamics (SPH) code by Razoumov & Sommer-Larsen (2007, 2006) and has found evolving escape fractions, with $f_{esc} = 6$ to 10 per cent at $z = 3.6$ decreasing to 1 to 2 per cent at $z = 2.4$. This simulation did not include the effects of dust.

Our SAMs predict the emissivity from star-forming galaxies down to a minimum rest-frame wavelength of 100 Å. Lyman-continuum photons are attenuated by a factor $f_{esc,H I}$; this determines the absorption of photons shortwards of 912 Å and is a non-evolving input to our radiative transfer code. This parameter is defined as the following ratio of intrinsic and observable luminosities at 912 and 1500 Å:

$$f_{esc,H I} = \frac{(L_{912}/L_{1500})_{escaping}}{(L_{912}/L_{1500})_{intrinsic}} = f_{esc} f_{1500}^{-1}, \tag{7}$$

where f_{esc} is the absolute attenuation factor from both dust and H I for ionizing photons near the Lyman limit, and f_{1500} is the factor from dust alone at 1500 Å. As dust absorption is an evolving effect included in the SAM, total absorption f_{esc} for ionizing photons escaping from galaxies must be interpreted as the product of $f_{esc,H I}$ and the average f_{1500} for a particular redshift in the model. The average value of f_{1500} in our model is higher at high redshift, and is higher in the low model than in the fiducial model at high redshift. Typical values of f_{1500}^{-1}, as seen in the difference between attenuated and unattenuated curves in Fig. 1, vary from about 6.8 at $z = 2$ to 11.2 at $z = 5$ for our fiducial model, and 9.7 to 14.2 in the low model. As noted in Gnedin et al. (2008), taking the total absorption to be a product of the dust and H I factors may not be physically realistic, as the two components may not be distributed in the same way within the galaxy, however it is sufficient for the purpose of calculating emissivities, as we are dealing only with global quantities.

2.5 Quasar emissivity

Quasar input to our model is accomplished using an assumed UV luminosity density, which determines the output at all energies via a fixed spectral form. We have used the quasar LFs at 912 Å determined by Hopkins, Richards & Hernquist (2007, HRH07) which are based on a large observational data set and spectral and obscurational modelling. This work found that, with the appropriate corrections for obscuration, a single bolometric function could match data in each band. Both the bright- and faint-end slopes of the LF are argued to become more shallow at higher redshift, indicating an increasing contribution from bright, unobscured AGN, which dominate the total AGN luminosity above redshift $\sim$2.

Another approach to modelling the quasar contribution to the background was presented in SB03. This work estimated the evolution of the unobserved faint-end of the quasar LF at high redshift using observational constraints on the ionizing background. They found very different results depending on whether they used constraints on the ionizing background from the quasar proximity effect or from the Lyman-α flux decrement method. Assuming the broken power law universal quasar spectrum, we present below that the HRH07 luminosity density evolution at 912 Å is similar to model A of SB03, which produced the lowest fluxes and was found to be consistent with the flux decrement data when combined with a substantial contribution from star-forming galaxies. The highest derived flux, arising in model C, was sufficient to produce ionizing
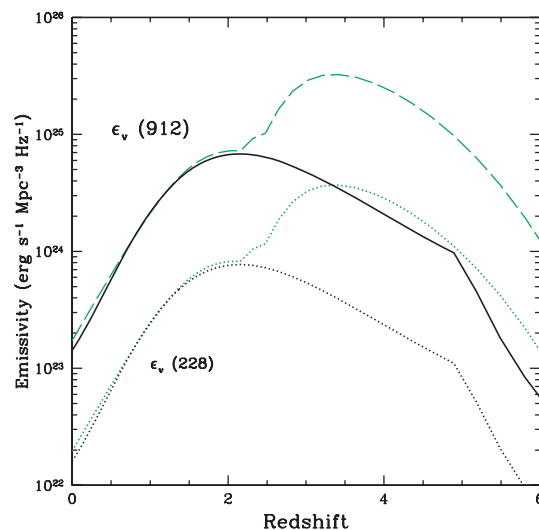

Figure 6. Quasar luminosity density for the Hopkins et al. (2007) (solid black) and Schirber & Bullock (2003) model C (broken green) models at 912 (upper lines) and 228 Å (lower lines). The latter has been multiplied by a factor of 0.8 to better match the observations at low redshift.

photons at the level suggested by proximity effect measurements. While we recognize that it is probable that many of these proximity effect measurements overestimate the background due to aforementioned biases, we will use the SB03 model C for the purposes of creating and analysing an extremely quasar-dominated background model.

Luminosity densities at the H I and He II Lyman limits for each of these models are shown in Fig. 6. We have renormalized the original model proposed by SB03 by a factor of 0.8 to better match the HRH07 results below redshift 2.3.

Quasars are assumed to have a spectrum which can be modelled as a broken power law in $F_\nu = dF/d\nu$. In the extreme UV, we have adopted the hard spectrum suggested by Telfer et al. (2002), from observations with the Faint Object Spectrograph on *HST* of quasars at a wide variety of non-local redshifts ($z > 0.33$). The values we assume are as follows:

$$F_\nu \propto \nu^{-\alpha} \tag{8}$$

with indices

$\alpha = 0.4 \quad (12\ \mu m < \lambda),$

$\alpha = 1.3 \quad (1\ \mu m < \lambda < 12\ \mu m),$

$\alpha = 0.2 \quad (500\ nm < \lambda < 1\ \mu m),$

$\alpha = 0.5 \quad (120\ nm < \lambda < 500\ nm),$

$\alpha = 1.57 \quad (\lambda < 120\ nm)$ and

$\alpha = 0.9 \quad (soft\ X\text{-rays}, > 500\ eV).$

The contribution of quasars to the background is only non-negligible in the extreme-UV ($\lambda < 120\ nm$). At other wavelengths, we use slopes to roughly fit typical X-ray spectra of Seyfert 1 galaxies, and the optical and IR emission of quasars seen in SDSS and other observations (Sanders et al. 1989; Vanden Berk et al. 2001).

3 COSMOLOGICAL MODELS AND RESULTING UV BACKGROUND

To calculate the evolving background radiation field, we have combined three estimates of the SFR density with two possible forms
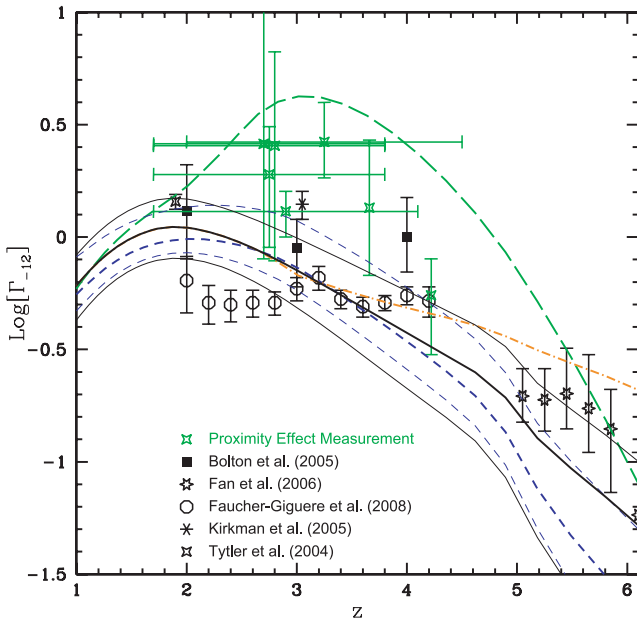
Figure 7. Ionization rate per hydrogen atom (with units of 10^{-12} s^{-1}) in our four scenarios compared with data at a range of redshifts. Black solid lines: fiducial model with H I escape fractions from star-forming galaxies of 0.02, 0.1 and 0.2 (bottom to top). Dashed blue lines: low star formation model, with escape fractions 0.1, 0.2 and 0.5. Orange dash–dotted line: high-peaked SFR with escape fraction 0.1. These aforementioned models all use the quasar emissivity of HRH07. The long-dashed green line shows the fiducial SFR model with quasar model C of Schirber & Bullock (2003), and escape fraction 0.02. Data points are divided into those obtained from flux-decrement analysis (black) and those obtained via proximity effect near quasars (green). References for the former are Bolton et al. (2005), Fan et al. (2006), Faucher-Giguère et al. (2008a), Kirkman et al. (2005), Tytler et al. (2004) and the latter include Scott et al. (2000), Cooke, Espey & Carswell (1997), Giallongo, Fontana & Madau (1997), Cristiani et al. (1995), Williger et al. (1994), Lu, Wolfe & Turnshek (1991), Bajtlik, Duncan & Ostriker (1988). Some points have been shifted slightly for readability.

for the quasar luminosity density. The two quasar models are the 'realistic' estimate of HRH07 from a large body of observational data, and a higher 'extreme' model motivated by proximity effect measurements for $3 < z < 5$ from SB03. Our four models are summarized in Table 1.

3.1 Lyα forest constraints

Inferred ionization rates and column density measurements from the Lyα forests of quasar spectra provide us with an independent measurement of the UV background through its ionizing properties, which we can compare with the IGM state computed by our radiative transfer code. In Fig. 7, we compare the ionization rate (in terms of Γ_{-12}, the average rate per hydrogen ion with units of 10^{-12} s^{-1}) with data from both the quasar proximity effect and the flux decrement in Lyα forest measurements. As discussed in the Introduction, these two techniques have tended to give disparate values for Γ_{-12}. For the fiducial and low models with the HRH07 QSO LF, we show ionization rates with several values for the escape fraction of ionizing radiation from the galactic H I disc. With a moderate H I escape fraction of 0.1 to 0.2, our fiducial model is able to reproduce the level of ionizing background detected by most determinations using flux decrement techniques. Including attenuation by dust, this corresponds to a total ionizing escape fraction of ∼1

to 3 per cent, consistent with upper limits from observations as well as values suggested by simulations (Razoumov & Sommer-Larsen 2007; Gnedin et al. 2008). With the low model, a higher H I escape fraction of ∼0.5 is necessary to match the highest redshift points ($z > 5$), due to the rapidly declining SFR at high redshift. This escape fraction is higher than suggested by some authors, but there are no direct constraints on escape fractions at such high redshifts.

Based on the quality of fits for our different models to these flux decrement data, we have chosen escape fractions of 0.1 and 0.2 for our fiducial and low models, respectively, as reasonable values to use in calculating the background and pair production opacity. Both of these models predict ionization rates which decline above redshift 2.5; this is due both to the shape of the SFH and the increasing opacity of the IGM with redshift.

The flux decrement calculations from the largest quasar samples (Faucher-Giguère et al. 2008a; Bolton et al. 2005) find ionization rates that are essentially flat from $z = 2$ out to 4, albeit with differing normalizations. Our model predictions are reasonably consistent with these observational estimates, considering the uncertainties involved. The high-peaked model better reproduces the flatness of the ionization rate from $z \sim 3$ to 4, but still predicts too steep a rise with time from $z \sim 2$ to 3. The SFH predicted by our fiducial model could be made perfectly consistent with the Faucher-Giguère et al. (2008a) data by assuming an escape fraction that evolves from ∼0.2 at $z \sim 4$ to 0.02 at $z \sim 2$.

The final scenario we examine uses the higher quasar emissivities of model C in Schirber & Bullock (2003). As the ionizing contribution from star formation is subdominant at all intermediate redshifts in this case, we have assumed a low escape fraction of 0.02. The ionizing flux in this model is capable of reproducing the highest measurements from the proximity effect. We have already mentioned several known biases which may have artificially elevated these values, and this model should be considered an extreme possibility.

Another Lyα forest measurement which can provide insight into the UV background is the relative abundance of H I and He II present in the IGM. This may be presented in terms of relative column densities $N(\text{He II})/N(\text{H I})$, or analogously as inverse ionization rates for these components $\Gamma_{\text{H I}}/\Gamma_{\text{He II}}$; this is often referred to as the UV softness parameter. In Fig. 8, we show how softness evolves with redshift for each of our background models. Our low, fiducial and high-peaked star formation densities with the HRH07 QSO LF are able to provide a reasonable match to observations when a moderate escape fraction is assumed. High escape fractions ≥0.5, which are required for the 'low' SFR model to match ionization rates at high redshift, tend to overpredict softness. Our quasar-dominated model (SB03, model C) does not reproduce the trend of increasing softness in the background field with redshift, another factor which disfavours such a dominant contribution from faint quasars. The column density ratio in this case is not found to be sensitive to the H I escape fraction.

3.2 The background flux

The key result of this work is a prediction of the evolving UV background out to redshift $z \sim 9$, which has been calculated from our models for the total (stellar + quasar) emissivity $\epsilon(\nu, z)$ combined with a calculation of the absorption and re-emission by IGM radiative transfer processes. Photons at non-ionizing wavelengths evolve passively, and are not attenuated significantly by any source. For these photons, the flux at a redshift z_0 and frequency ν_0 in proper
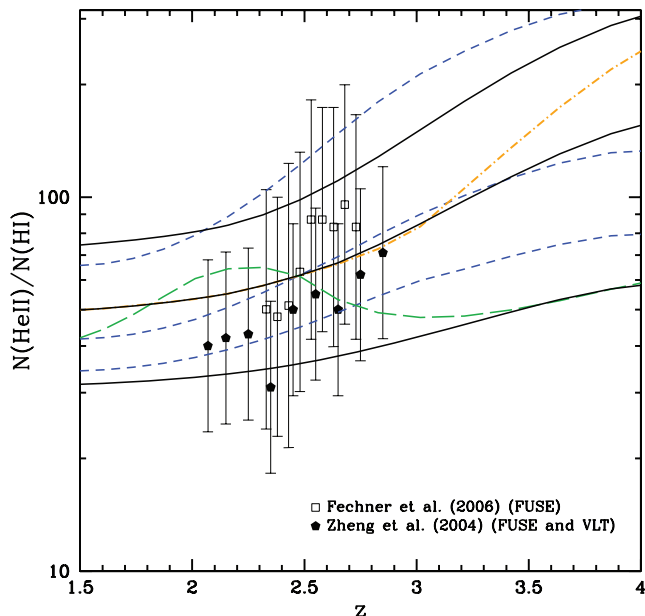
Figure 8. The ratio of He II to H I column densities plotted against redshift. Higher values indicate a softer ionizing background, with comparatively more ionizing photons available per hydrogen atom. Line types in this plot are the same as in Fig. 7. Data are from observations of He II Lyα systems by Zheng et al. (2004) and Fechner et al. (2006).

coordinates can be written as (Peebles 1993)

$$J(\nu_0, z_0) = \frac{1}{4\pi} \int_{z_0}^{\infty} \frac{dl}{dz} \frac{(1+z_0)^3}{(1+z)^3} \epsilon(\nu, z) e^{-\tau_{\text{eff}}} \, dz, \qquad (9)$$

where $\nu = \nu_0(1 + z)/(1 + z_0)$ and dl/dz is the cosmological line element, defined as

$$\frac{dl}{dz} = \frac{c}{(1+z)H_0} \frac{1}{\sqrt{\Omega_m(1+z)^3 + \Omega_\Lambda}} \qquad (10)$$

for a flat Λ cold dark matter (ΛCDM) universe. Here τ_{eff} is the optical depth for ionizing radiation due to Poisson-distributed HI absorption systems, defined as (Madau et al. 1999)

$$\tau_{\text{eff}}(\nu_0, z_0, z) = \int_{z_0}^{z} dz' \int_0^{\infty} dN_{\text{HI}} \frac{\partial^2 N}{\partial N_{\text{HI}} \partial z'} (1 - e^{-\tau}), \qquad (11)$$

where τ is the Lyman continuum optical depth through a given cloud, and $\partial^2 N/(\partial N_{\text{HI}} \partial z)$ is the absorber distribution that we specified for our model in equation (3). For non-ionizing radiation, the effective opacity is zero. At wavelengths well above the Lyman limit, the background at a redshift z_0 is determined by the total history of emission at higher redshifts $z > z_0$. At ionizing wavelengths, the mean free path of photons is shorter than cosmological distances at redshifts greater than the breakthrough redshift, and therefore the ionizing background at $z_0 > z_{br}$ is determined by the emissivity of approximately contemporary sources.

In Fig. 9, we present the $z = 0$ EBL flux for our SAMs, alongside two other recent EBL determinations using alternate methods. At low redshift, the effect of our high quasar and high-peaked star formation models on the total background are negligible, and are not shown. We have shown the EBL calculated out to the far-IR in this plot, though results at wavelengths longer than the optical near-IR peak at ~1 μm are not relevant to gamma-ray opacities in the high-redshift regime we discuss here. Dust re-emission of light in this model is based upon the IR templates of Devriendt & Guiderdoni (2000). Much more detailed IR background modelling,
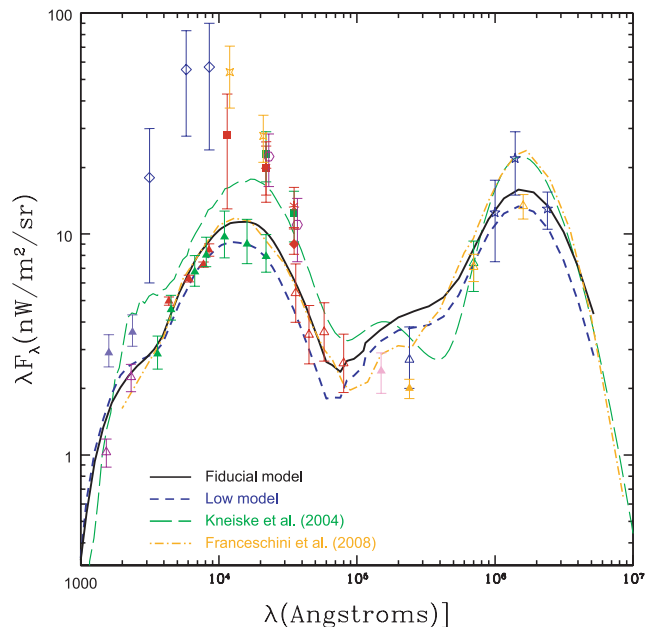

Figure 9. The predicted $z = 0$ EBL spectrum from our SAMs of galaxy formation from the UV to far-IR (see also Primack et al. 2008). We show results for the fiducial (black) and low (dashed blue) models, compared with experiments at a number of wavelengths. Other lines show the EBL models of Franceschini et al. (2008) and Kneiske et al. (2004) for comparison. The blue–violet triangles are results from STIS on *HST* (Gardner et al. 2000), while the open magenta triangles are from *GALEX* (Xu et al. 2005). The green and red triangles are from the Hubble Deep Field (Madau & Pozzetti 2000) and Ultra Deep Field (Dolch, in preparation) respectively; the former also includes near-IR ground-based data. Open red triangles are from IRAC on *Spitzer* (Fazio et al. 2004). The blue diamonds are Bernstein (2007) and other symbols in the near-IR are from several analyses of DIRBE data at 1.25, 2.2 and 3.5 μm (Gorjian, Wright & Chary 2000; Wright & Reese 2000; Cambrésy et al. 2001; Levenson et al. 2007; Levenson & Wright 2008). In the mid-IR, counts data is shown from *ISO* (Elbaz et al 2002) and *Spitzer* (Chary et al. 2004; Papovich et al. 2004; Dole et al. 2006; Frayer et al. 2006). In the far-IR, direct detection data is shown from DIRBE (Wright 2004, blue stars).

taking into account the latest *Spitzer* data, will be presented in Gilmore et al. (in preparation).

Understanding the evolution of the background field is critical to our calculation of the absorption of gamma rays, as the flux at high redshift can be both significantly higher than and of a different spectral shape than the local background. In Fig. 10, we show the background flux for our four models at several redshifts, including $z = 0$ where we have also shown a compilation of observable data, including estimates from both absolute photometry and discrete source number counts. In each case, we assume the 'best-fitting' escape fractions of Table 1, which we have chosen based on the comparisons with Lyα forest measurements. At all redshifts, the background shows a sharp drop at the Lyman edge; this is a combined consequence of absorption in stellar atmospheres, H I in galaxies (quantified as $f_{\text{esc,HI}}$ in our models), and IGM reprocessing. The feature at ~300 Å is due to He II Lyα.

4 GAMMA-RAY ATTENUATION

Gamma rays can interact with background photons if sufficient energy exists in the centre of mass to create an electron–positron
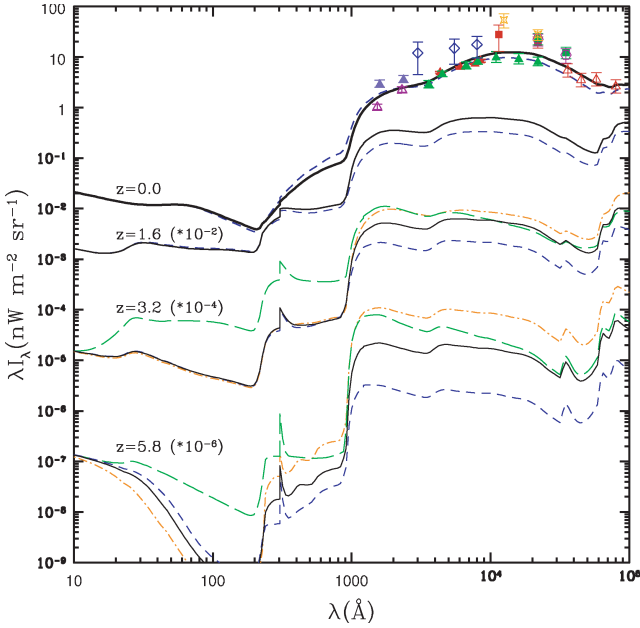
Figure 10. The history of the background flux, shown at the present day and three other redshifts. Intensities at the non-zero redshifts have been multiplied by the indicated factors (10^{-2}, 10^{-4} and 10^{-6} at $z = 1.6$, 3.2, 5.8, respectively) to separate the lines. Black solid line: fiducial model with H I escape fraction of 0.1. Dashed blue line: low star formation model, with escape fraction 0.2. Orange dash–dotted line: high-peaked SFR with escape fraction 0.1. Green long-dashed: fiducial model with SB03 quasar contribution and escape fraction 0.02. At low redshift, only the first two models are shown, as the other models do not produce discernibly different levels of background at these times. We have also shown observational measurements of the background flux at $z = 0$ in the UV, optical and near-IR from Fig. 9.

pair with total mass $2m_e$:

$$\sqrt{2E_1 E_2(1 - \cos\theta)} \geq 2m_e c^2, \tag{12}$$

where E_1 and E_2 are the photon energies and θ is the angle of incidence. A gamma ray of energy E_γ can, therefore, pair produce with background photons above a threshold energy of

$$E_{th} = \frac{2m_e^2 c^4}{E_\gamma(1 - \cos\theta)}. \tag{13}$$

The cross-section for this process is (Madau & Phinney 1996)

$$\sigma(E_1, E_2, \theta) = \frac{3\sigma_T}{16}(1 - \beta^2)$$
$$\times \left[2\beta(\beta^2 - 2) + (3 - \beta^4)\ln\left(\frac{1 + \beta}{1 - \beta}\right)\right], \tag{14}$$

where

$$\beta = \sqrt{1 - \frac{2m_e^2 c^4}{E_1 E_2(1 - \cos\theta)}}, \tag{15}$$

and σ_T is the Thompson scattering cross-section. The cross-section is maximized for centre of mass energies of approximately twice the threshold energy $2m_e c^2$, and falls as approximately as inverse energy for $E \gg E_{th}$. The likelihood of absorption is maximized for photons at about four times the absolute threshold energy, with one factor of 2 from σ and another in going from $\theta = \pi$ ('head-on' configuration) to the most probable angle of interaction $\theta \approx \pi/2$. Gamma rays above 1 TeV are most attenuated by the near- and mid-IR range of the EBL, while those in the 300 GeV to 1 TeV regime are sensitive to light in

the near-IR and optical. Below 200 GeV, it is mainly UV photons that have sufficient energy to cause the pair production interaction. Below 19 GeV, only background photons with energies above the Lyman limit have sufficient energy to interact at any angle in the rest frame, and there is little attenuation. Note that these numbers refer to rest-frame energy of the gamma ray, which can be substantially higher than its observed energy due to redshifting. If the differential number density of background photons at energy E_{bg} is $n(E_{bg}, z)$, then the optical depth of attenuation for a photon of observed energy E_γ is

$$\tau(E_\gamma, z_0) = \frac{1}{2}\int_0^{z_0} dz \frac{dl}{dz} \int_{-1}^{1} d(\cos\theta)(1 - \cos\theta)$$
$$\times \int_{E_{min}}^{\infty} dE_{bg} \, n(E_{bg}, z) \, \sigma[E_\gamma(1 + z), E_{bg}, \theta], \tag{16}$$

where we have

$$E_{min} = E_{th}(1 + z)^{-1} = \frac{2m_e^2 c^4}{E_\gamma(1 + z)(1 - \cos\theta)}$$

and dl/dz is the cosmological line element defined in equation (10).

For each of our four models, we have calculated the optical depth of gamma rays at all relevant energies and redshifts. As in our calculation of the background flux above, we assume the H I escape fractions listed in Table 1. It should be emphasized that the choice of escape fraction has little effect on absorption of gamma rays at energies >10 GeV. We find, as argued in Oh (2001), that the background field at energies above 1 Ry is negligible as a barrier to cosmological gamma rays, and that significant optical depth above this energy is due to photons longwards of the Lyman limit, where photon density increases dramatically in all of our models. While gamma rays are limited to interactions with background photons of an absolute minimum energy $E_{th} = m_e^2 c^4/E_\gamma$ (with $\cos\theta = -1$), redshifting places these gamma rays at higher energies at earlier epochs, where they can pair produce on the non-ionizing background. The increase of SFR density by roughly an order of magnitude between present-day and peak rates means that gamma rays from high-redshift sources will tend to be attenuated most strongly at these early redshifts, where they have energies $(1 + z)$ times higher than at $z = 0$.

In Fig. 11, the optical depth versus gamma-ray energy is shown for each model at various redshifts. These high-redshift results should be considered complementary to our other calculations of EBL with these SAMs, which emphasized the absorption of >100 GeV gamma rays at lower redshift. The effect of the UV background is to produce a relatively sharp and featureless cut-off in energy. At energies above 100 GeV, the effect of the EBL has often been quantified as a change in the spectral index of observed blazar spectra (e.g. Aharonian et al. 2006), due to the relatively flat number density of EBL photons in the near and mid-IR. At lower energies, this approximation is not valid over any significant range in energy, due to the steepness of the cut-off that results in rapidly increasing numbers of photons with increasing wavelength in the UV.

Our high-peaked SFRD and quasar-dominated models give absorption features that are similar, despite being very different in terms of the spectral form of the background flux. While the emission from quasars produces a much higher ionizing background, the spectral cut-off at all redshifts we have explored is dominated by the photons longwards of the Lyman limit.

In Fig. 12, we show the redshifts at which the universe becomes optically thick ($\tau > 1$) to gamma rays of a given energy for each

Table 2. Here we summarize a broad set of models, and the qualitative level of agreement of each with Lyα forest data, proximity effect measurements and simulations of total ionizing escape fraction from star-forming galaxies. The numbers of the models shown in Figs 10–12 are in bold.

| | Model parameters | | | | Fits with data | | |
Model	SFR density	Quasar luminosity	f_{escHI}	Flux decrement[a]	Proximity effect[b]	Softness[c]	f_{esc} [d]
1.1	Fiducial	HRH07	0.02	x	x	○	√
1.2	Fiducial	HRH07	0.10	○	x	√	√
1.3	Fiducial	HRH07	0.20	○	x	○	√
2.1	Low	HRH07	0.10	x	x	○	√
2.2	Low	HRH07	0.20	○	x	√	√
2.3	Low	HRH07	0.50	○	x	○	○
3	Fiducial high-peaked	HRH07	0.10	√	x	√	√
4	Fiducial	SB03 model C	0.02	x	√	x	√

√ = best agreement; ○ = marginal agreement; x = poor agreement.
[a]This refers to the relatively flat ionization rate for H I at a level seen in the quasar spectra data of Bolton et al. (2005) and Faucher-Giguère et al. (2008a) (Fig. 7).
[b]The higher levels of ionization rate determined in uncorrected proximity effect measurements (Fig. 7).
[c]The softness $\eta \equiv N(\text{He II})/N(\text{H I})$, from data compiled in Fig. 8.
[d]The total escape fraction; recall from Section 2 that this is equivalent to $f_{\text{esc,H I}} * f_{1500}$. In our SAMs, f_{1500}^{-1} ranges from about 7 to 14 at the redshifts of interest.

of our models. From this plot, we can see in a general sense how background attenuation affects different energy regimes at different redshifts. The low model shows little change at redshifts higher than about 3, due to the rapid decline in star formation after this point. The high-peaked model has the most impact at high redshift, and produces absorption features that evolve out to $z > 6$.

5 DISCUSSION

We have created and analysed predictions for the UV background that are intended to broadly span the possibilities in SFR and quasar-luminosity density. Our fiducial model with the HRH07 QSO LF (first entry in Table 1) provides a reasonable match to the level of ionizing flux inferred from Lyα forest measurements when an H I escape fraction of 0.1 is assumed; this corresponds to a total f_{esc} of 1 to 1.5 per cent when combined with the dust absorption values predicted by our semi-analytic galaxy formation model. The 'low' model for the SFR density, with the lower CDM power spectrum normalization of *WMAP*3, requires a larger escape fraction to match ionization rate data, especially the higher redshift points $z > 5$, where $f_{\text{esc,H I}} \sim 0.5$ is required. Both of these models fail to reproduce the nearly constant ionization rate between $2 < z < 4.5$ seen in some flux decrement analyses. The high-peaked model, which has a SFR that increases until redshift 5, does produce a somewhat flatter ionization rate, as suggested by Faucher-Giguère et al. (2008b). The large amount of high-redshift star formation in this model is not supported by estimates of stellar mass buildup, and should be considered a somewhat extreme scenario. Another mechanism for producing a flatter ionization rate history is an evolving escape fraction that increases with redshift, a possibility that we do not explore here but which has been seen in some simulations (Razoumov & Sommer-Larsen 2007, 2006), and as already mentioned may be suggested by observations which have detected Lyman continuum radiation from distant ($z \sim 3$) galaxies (Shapley et al. 2006), but not closer sources (Siana et al. 2007). This would have only a weak effect on the opacities we have calculated, as most attenuation of gamma rays is due to the non-ionizing UV background, which would have a much larger number density than the ionizing background even for a high escape fraction.

Our results suggest that observations of sufficient numbers of high-energy gamma-ray sources out to high redshift could provide a probe of the UV background at these epochs that is independent of any other observational test. Pair production with target background photons produces a spectral cut-off at energies that are dependent upon redshift and assumed cosmological model. With enough detections of blazars and/or GRBs at different confirmed redshifts in the 10 to 100 GeV energy decade, it should be possible to detect an evolving cut-off in energy, and distinguish between the different background levels proposed in this work. The exact number of blazars that will be detected at GeV energies over the coming years is uncertain and dependent upon the poorly understood emission processes and number density evolution of these sources. However, even conservative estimates indicate that a large number of sources will be detectable by the *Fermi* \ spacecraft, which was launched in 2008 June and is currently in all-sky survey mode. The EGRET experiment on the *Compton Gamma-ray Observatory* (*CGRO*) detected more than 60 high-confidence blazars at energies of >100 MeV out to redshift 2.28, mostly of the FSRQ type (Mukherjee et al. 1997). An extrapolation of these results suggests that *Fermi* will see ∼1000 blazars extending to higher redshift (Dermer 2007). An analysis of two different realizations of the blazar LF by Chen, Reyes & Ritz (2004) suggested that *Fermi* could detect thousands of blazars, and would potentially be able to measure attenuation at distances as great as $z = 5$. The 3 month *Fermi* LAT survey has already reported 106 AGN sources at high confidence (Abdo et al. 2009). In addition to analysing blazar spectra in survey and pointed observations, *Fermi* will also act as a finder for new and upcoming ground-based experiments such as HESS-II and MAGIC-II which will be capable of resolving most of the energy ranges of interest. In survey mode, *Fermi* will also act as an alert system for flaring sources.

None of our models predicts significant attenuation at 10 GeV or below for any redshift. This is true even for our extremely quasar-dominated model, where the opacity of a 10 GeV observed gamma ray is never higher than $\tau \sim 0.2$. As the ionizing flux in this model is higher than allowed by most measurements of the Lyα forest, it is unlikely that any cosmological model could produce significant gamma-ray opacity due to a large contribution of ionizing photons to the background. The high-peaked star formation model produces
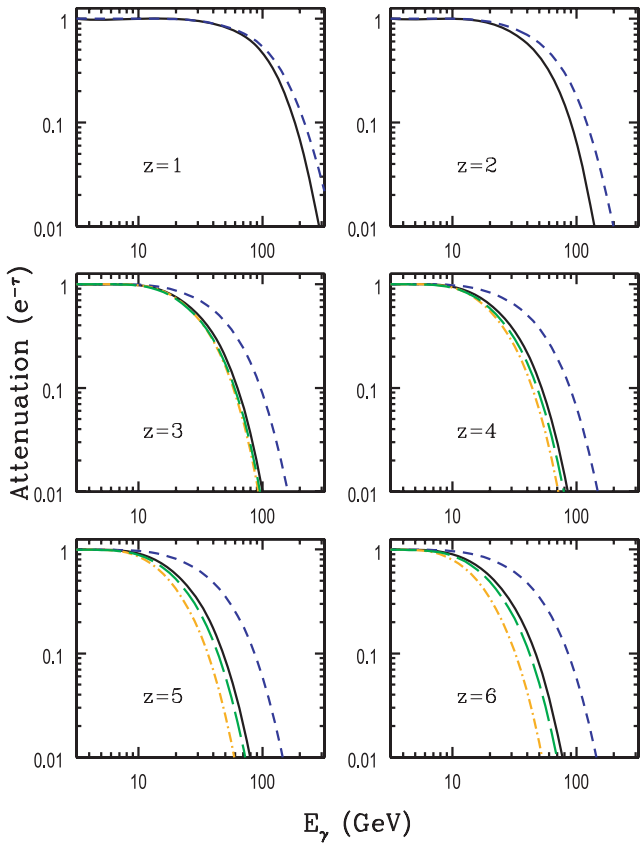
Figure 11. Attenuation factors ($e^{-\tau}$) as a function of gamma-ray energy for the indicated source redshifts. Curves are as in Fig. 10, and indicate the absorption resulting from our models of star formation and quasar emissivity. Black solid line: fiducial model with H I escape fraction of 0.1. Dashed blue line: low star formation model, with escape fraction 0.2. Orange dash–dotted line: high-peaked SFR with escape fraction 0.1. Green long-dashed: fiducial model with SB03 quasar contribution and escape fraction 0.02. Curves for the high-peaked star formation and high quasar models converge to the fiducial model for $z \leq 2$.

the most absorption in the 10–100 GeV energy range for $z > 3$, but despite having a very high UV output only has a moderate impact on the calculated optical depths relative to the fiducial model.

5.1 Comparison with other work

It is useful to compare the absorption predicted by our models with the calculations of other authors who have used different methods, in the cases where their results include our energy and redshift regime of interest. In many instances, our predicted attenuation is less than what has been previously proposed.

The background model of Franceschini et al. (2008) is based upon extrapolated LFs determined from a large compilation of multiwavelength data, including deep ACS imaging of distant galaxies, and treats separately the evolutionary histories of spiral, elliptical and star-bursting galaxy populations. While their EBL agrees well with our fiducial model at $z = 0$ and 1 (Gilmore et al. in preparation), their absorption τ in the 10–100 GeV energy decade is at least a factor of 2 greater at $z = 2$–4 than any of our models. The most recent models of Stecker and collaborators (Stecker, Malkan & Scully 2006, 2007) are based on a 'backward evolution' model in which galaxies' emission SEDs are determined by their brightness in one band, taken to be 60 μm. The luminosity of the galaxy population
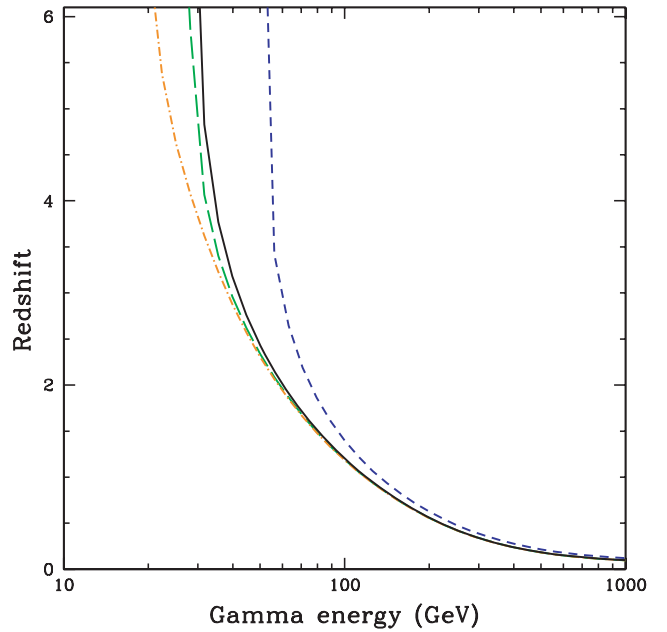

Figure 12. The redshifts at which the universe becomes optically thick ($\tau > 1$) to gamma rays at a given observed energy. Line colours and types are as in Fig. 11.

at this wavelength is assumed to brighten with redshift as a power law in $(1 + z)$. One disadvantage of this method is that it attempts to describe luminosity evolution over several orders of magnitude in wavelength from a single broken power law, which cannot take into account the complexity of galaxy evolution. Gamma-ray opacities in this work are much higher than our predictions, with the universe optically thick ($\tau > 1$) to 10 GeV gamma rays above $z \sim 3$, and for >25 GeV above $z = 1$. This level of absorption holds very different implications for experiments such as *Fermi*. At high redshifts, absorption cut-off spectral features would be visible between about 5 and 20 GeV, with no signal from higher energies due to optical thickness from the background. The galaxy SEDs in these models have no emission above Lyman energies, and therefore all attenuation at these very low energies is the result of near-threshold interactions with non-ionizing UV photons. The redshift-dependent optical and UV SEDs used are based on the population synthesis models of Bruzual & Charlot (1993). This model does not include UV dust extinction, which as we have found in this work can reduce far-UV emissivity by a factor of ~10 at higher redshifts.

The recent observation by *Fermi* of high-energy emission from GRB 080916C at $z = 4.35$ (Greiner et al. 2009a) provides a valuable first test of these predictions for GeV absorption. The highest energy photon seen by the LAT was 13.2 GeV, with over 10 photons seen above 1 GeV (Abdo et al. 2009). In all of our models, the gamma-ray optical depth is much less than 1 for this energy and redshift, and similar values are found in the star formation models of Razzaque et al. (2009). The models of Stecker and collaborators predict a much higher opacity, $\tau = 3.5$ to 4.5, for the 13 GeV photon. Including the 1σ error on redshift and photon energy in finding maximal and minimal values, the corresponding transmission probability could be as high as 8.2 per cent for their 'baseline' model, or as low as 0.5 per cent for the 'fast evolution' model (Stecker, private communication). While it is difficult to draw conclusions from a single event, more bursts seen with GeV emission equal or greater to GRB 080916C could strongly disfavour such a large background flux, and observations of slightly higher energy photons

($E \sim 30$ GeV) from similar redshifts could provide a test of our models.

5.2 Caveats and future work

We expect our approach to be reasonably accurate at predicting the ionizing and non-ionizing background fields out to redshift ~ 6, where H I Gunn–Peterson troughs appear in observed quasar spectra (Fan et al. 2006). At higher redshifts, during the epoch of reionization, the concept of a uniform background for ionizing photons is no longer valid, as photons above the Lyman limit are confined to the vicinity of their sources. In our Lyman absorption model (equation 3), the sudden increase seen in H I opacity at redshift six is not represented, and our model would, therefore, be expected to overproduce the ionizing background above this redshift. A similar limitation exists in our treatment of He opacities above the redshift of He reionization $z \sim 3$. However, these factors alone are unlikely to have a significant effect on calculated opacities.

We have made the assumption of a universal stellar IMF in this work, and have not included a separate population of metal-free (Population III) stars or other early source types such as mini-quasars (Madau et al. 2004). These types of unobserved sources could have very different spectra than standard stellar populations, and could produce large contributions to the ionizing and non-ionizing UV backgrounds. Because of redshift effects, gamma rays with low (<10 GeV) observed energies for very high-redshift sources could have significant interactions with the freely propagating non-ionizing background. It is, therefore, possible that opacities at reionization redshifts could be much higher than we propose here due to unseen UV production mechanisms. While models for gamma-ray blazars do not typically predict sources at these high redshifts, GRBs are known to exist above redshift six (Greiner et al. 2009b), and long-duration GRBs could potentially be seen as far out as star formation occurs. The EGRET experiment, operating from 30 MeV up to ~ 30 GeV, was able to view a small number of photons from GRBs, and the detection of high-energy emission from GRB 080916C by the *Fermi* LAT demonstrates the ability of this instrument to detect GeV photons from these events. Though predictions are highly uncertain, it is possible that GRBs could produce significant numbers of photons well above 10 GeV through inverse-Compton or hadronic processes (Le & Dermer 2009; Ando, Nakar & Sari 2008). Calculations of the background flux from some possible reionization scenarios and source types at $z > 6$ may, therefore, be a worthwhile undertaking.

It has been suggested by a number of authors that the discrepancy between observed stellar mass density and instantaneous SFR density (see Section 2.2) could be explained by an IMF that evolves with redshift or is more top-heavy in rapidly star-forming galaxies (Baugh et al. 2005; Fardal et al. 2007; Davé 2008). Alternatively, an IMF with shallower high-end slope has been suggested as a source of early reionization (Chary 2008). Altering the high-mass end of the IMF will change the spectrum produced by galaxies and also the attenuation by dust, although as probes of star formation generally involve the same high-mass stars that produce the UV background, there is some degree of degeneracy between these two quantities when the assumed IMF is changed. This is also an issue that warrants further study.

REFERENCES

Abdo A. A. et al., Sci, 2009, 323, 1688
Aharonian F. et al., 2006, Nat, 440, 1018
Albert J. et al., 2008, Sci, 320, 1752
Ando S., Nakar E., Sari R., 2008, ApJ, 689, 1150
Bajtlik S., Duncan R. C., Ostriker J. P., 1988, ApJ, 327, 570
Barger A. J., Cowie L. L., Mushotzky R. F., Yang Y., Wang W.-H., Steffen A. T., Capak P., 2005, AJ, 129, 578
Baugh C. M., Lacey C. G., Frenk C. S., Granato G. L., Silva L., Bressan A., Benson A. J., Cole S., 2005, MNRAS, 356, 1191
Bechtold J., 1994, ApJS, 91, 1
Bernstein R. A., 2007, ApJ, 666, 663
Bernstein R. A., Freedman W. L., Madore B. F., 2002a, ApJ, 571, 56
Bernstein R. A., Freedman W. L., Madore B. F., 2002b, ApJ, 571, 107
Bolton J. S., Haehnelt M. G., 2007, MNRAS, 382, 325
Bolton J. S., Haehnelt M. G., Viel M., Springel V., 2005, MNRAS, 357, 1178
Bouwens R. J., Illingworth G. D., Franx M., Ford H., 2007, ApJ, 670, 928
Bouwens R. J., Illingworth G. D., Franx M., Ford H., 2008, ApJ, 686, 230
Boyle B. J., Shanks T., Croom S. M., Smith R. J., Miller L., Loaring N., Heymans C., 2000, MNRAS, 317, 1014
Brown M. J. I. et al., 2006, ApJ, 638, 88
Bruzual A. G., Charlot S., 1993, ApJ, 405, 538
Bruzual A. G., Charlot S., 2003, MNRAS, 344, 1000
Cambrésy L., Reach W. T., Beichman C. A., Jarrett T. H., 2001, ApJ, 555, 563
Cardelli J. A., Clayton G. C., Mathis J. S., 1989, ApJ, 345, 245
Charlot S., Fall S. M., 2000, ApJ, 539, 718
Chary R. R., 2008, ApJ, 680, 32
Chary R. R. et al., 2004, ApJS, 154, 80
Chen A., Reyes L. C., Ritz S., 2004, ApJ, 608, 686
Cooke A. J., Espey B., Carswell R. F., 1997, MNRAS, 284, 552
Cristiani S., D'Odorico S., Fontana A., Giallongo E., Savaglio S., 1995, MNRAS, 273, 1016
Croom S. M., Smith R. J., Boyle B. J., Shanks T., Miller L., Outram P. J., Loaring N. S., 2004, MNRAS, 349, 1397
Dahlen T., Mobasher B., Dickinson M., Ferguson H. C., Giavalisco M., Kretchmer C., Ravindranath S., 2007, ApJ, 654, 172
Dall'Aglio A., Wisotzki L., Worseck G., 2008, A&A, 491, 465
Davé R., 2008, MNRAS, 385, 147
Dermer C. D., 2007, ApJ, 659, 958
Devriendt J. E. G., Guiderdoni B., 2000, A&A, 363, 851
Dijkstra M., Haiman Z., Loeb A., 2004, ApJ, 613, 646
Dole H. et al., 2006, A&A, 451, 417
Elbaz D., Cesarsky C. J., Chanial P., Aussel H., Franceschini A., Fadda D., Chary R. R., 2002, A&A, 384, 848
Fan X. et al., 2001, AJ, 122, 2833
Fan X. et al., 2006, AJ, 132, 117
Fardal M. A., Katz N., Weinberg D. H., Davé R., 2007, MNRAS, 379, 985
Faucher-Giguère C.-A., Prochaska J. X., Lidz A., Hernquist L., Zaldarriaga M., 2008a, ApJ, 681, 831
Faucher-Giguère C.-A., Lidz A., Hernquist L., Zaldarriaga M., 2008b, ApJ, 682, L9
Fazio G. G. et al., 2004, ApJS, 154, 39
Fechner C. et al., 2006, A&A, 455, 91
Fixsen D. J., Dwek E., Mather J. C., Bennett C. L., Shafer R. A., 1998, ApJ, 508, 123
Franceschini A., Rodighiero G., Vaccari M., 2008, A&A, 487, 837
Frayer D. T. et al., 2006, ApJ, 647, L9
Gardner J. P., Brown T. M., Ferguson H. C., 2000, ApJ, 542, L79
Giallongo E., Fontana A., Madau P., 1997, MNRAS, 289, 629

Gilmore R. C., Madau P., Primack J. R., Somerville R. S., 2008, in Aharonian F. A., Hofmann W., Rieger F., eds, AIP Conf. Proc. Vol. 1085, High Energy Gamma-Ray Astronomy: Proc. Int. Meeting on High Energy Gamma-Ray Astronomy. Am. Inst. Phys., New York, p. 577

Gnedin N. Y., Kravtsov A. V., Chen H.-W., 2008, ApJ, 672, 765

Gorjian V., Wright E. L., Chary R. R., 2000, ApJ, 536, 550

Gould R. J., Schreder G. P., 1967, Phys. Rev., 155, 1404

Greiner J. et al., 2009a, A&A, 498, 89

Greiner J. et al., 2009b, ApJ, 693, 1610

Haardt F., Madau P., 1996, ApJ, 461, 20

Haardt F., Madau P., 2001, in Neumann D. M., Tran J. T. V., eds, Clusters of Galaxies and the High Redshift Universe Observed in X-rays, Modelling the UV/X-ray Cosmic Background with CUBA

Haehnelt M. G., Madau P., Kudritzki R., Haardt F., 2001, ApJ, 549, L151

Hauser M. G., Dwek E., 2001, ARA&A, 39, 249

Hauser M. G. et al., 1998, ApJ, 508, 25

Hopkins A. M., 2004, ApJ, 615, 209

Hopkins A. M., 2007, in Afonso J., Ferguson H. C., Mobasher B., Norris R., eds, ASP Conf. Ser., Vol. 380. Deepest Astronomical Surveys. The Star Formation History of the Universe. Astron. Soc. Pac., San Francisco, p. 423

Hopkins P. F., Richards G. T., Hernquist L., 2007, ApJ, 654, 731 (HRH07)

Hu E. M., Kim T.-S., Cowie L. L., Songaila A., Rauch M., 1995, AJ, 110, 1526

Iglesias-Páramo J., Buat V., Donas J., Boselli A., Milliard B., 2004, A&A, 419, 109

Jiang L. et al., 2006, AJ, 131, 2788

Kennicutt R. C. Jr. et al., 1998, ApJ, 498, 181

Kim T.-S., Hu E. M., Cowie L. L., Songaila A., 1997, AJ, 114, 1

Kirkman D. et al., 2005, MNRAS, 360, 1373

Kneiske T. M., Mannheim K., Hartmann D. H., 2002, A&A, 386, 1

Kneiske T. M., Bretz T., Mannheim K., Hartmann D. H., 2004, A&A, 413, 807

Komatsu E. et al., 2009, ApJS, 180, 330

Kriss G. A. et al., 2001, Sci, 293, 1112

Lagache G., Haffner L. M., Reynolds R. J., Tufte S. L., 2000, A&A, 354, 247

Le T., Dermer C. D., 2009, ApJ, 700, 1026

Levenson L. R., Wright E. L., 2008, ApJ, 683, 585

Levenson L. R., Wright E. L., Johnson B. D., 2007, ApJ, 666, 34

Liske J., Williger G. M., 2001, MNRAS, 328, 653

Loeb A., Eisenstein D. J., 1995, ApJ, 448, 17

Lu L., Wolfe A. M., Turnshek D. A., 1991, ApJ, 367, 19

Madau P., Haardt F., 2009, ApJ, 693, L100

Madau P., Phinney E. S., 1996, ApJ, 456, 124

Madau P., Pozzetti L., 2000, MNRAS, 312, L9

Madau P., Haardt F., Rees M. J., 1999, ApJ, 514, 648

Madau P., Rees M. J., Volonteri M., Haardt F., Oh S. P., 2004, ApJ, 604, 484

Mannucci F., Buttery H., Maiolino R., Marconi A., Pozzetti L., 2007, A&A, 461, 423

Matute I., La Franca F., Pozzi F., Gruppioni C., Lari C., Zamorani G., 2006, A&A, 451, 443

Milliard B., Donas J., Laget M., Armand C., Vuillemin A., 1992, A&A, 257, 24

Mukherjee R. et al., 1997, ApJ, 490, 116

Oh S. P., 2001, ApJ, 553, 25

Osterbrock D. E., 1989, Astrophysics of Gaseous Nebulae and Active Galactic Nuclei, University Science Books, Mill Valley, CA

Ouchi M. et al., 2004, ApJ, 611, 660

Papovich C. et al., 2004, ApJS, 154, 70

Peebles P. J. E., 1993, Principles of Physical Cosmology. Princeton Univ. Press Princeton

Primack J. R., Somerville R. S., Bullock J. S., Devriendt J. E. G., 2001, in Aharonian F. A., Völk H. J., eds, AIP Conf. Proc. Vol. 558, High Energy Gamma-Ray Astronomy: Int. Symp. Am. Inst. Phys., New York, p. 463

Primack J. R., Bullock J. S., Somerville R. S., 2005, in Aharonian F. A., Völk H. J., Horns D., eds, AIP Conf. Proc. Vol. 745, High Energy Gamma-Ray Astronomy: 2nd Int. Symp. on High Energy Gamma-Ray Astronomy. Am. Inst. Phys., New York, p. 23

Primack J. R., Gilmore R. C., Somerville R. S., 2008, in Aharonian F. A., Hofmann W., Rieger F., eds, AIP Conf. Proc. Vol. 1085, High Energy Gamma-Ray Astronomy: Proc. 4th Int. Meeting on High Energy Gamma-Ray Astronomy. Am. Inst. Phys., New York, p. 71

Rauch M. et al., 1997, ApJ, 489, 7

Razoumov A. O., Sommer-Larsen J., 2006, ApJ, 651, L89

Razoumov A. O., Sommer-Larsen J., 2007, ApJ, 668, 674

Razzaque S., Dermer C. D., Finke J. D., 2009, ApJ, 697, 483

Reddy N. A., Naveen A., Steidel C. C., Pettini M., Adelberger K. L., Shapley A. E., Erb D. K., Dickinson M., 2008, ApJS, 175, 48

Richards G. T., Vanden Berk D. E., Reichard T. A., Hall P. B., Schneider D. P., SubbaRao M., Thakar A. R., York D. G., 2002, AJ, 124, 1

Richards G. T. et al., 2006, AJ, 131, 2766

Salamon M. H., Stecker F. W., 1998, ApJ, 493, 547

Sanders D. B., Phinney E. S., Neugebauer G., Soifer B. T., Matthews K., 1989, ApJ, 347, 29

Schaye J., Aguirre A., Kim T.-S., Theuns T., Rauch M., Sargent W. L. W., 2003, ApJ, 596, 768

Schirber M., Bullock J. S., 2003, ApJ, 584, 110

Schirber M., Miralda-Escudé J., McDonald P., 2004, ApJ, 610, 105

Schiminovich D. et al., 2005, ApJ, 619, L47

Scott J., Bechtold J., Dobrzycki A., Kulkarni V. P., 2000, ApJS, 130, 67

Shapley A. E., Steidel C. C., Pettini M., Adelberger K. L., Erb D. K., 2006, ApJ, 651, 688

Shull J. M., Tumlinson J., Giroux M. L., Kriss G. A., Reimers D., 2004, ApJ, 600, 570

Siana B. et al., 2007, ApJ, 668, 62

Smette A., Heap S. R., Williger G. M., Tripp T. M., Jenkins E. B., Songaila A., 2002, ApJ, 564, 542

Somerville R. S., Primack J. R., 1999, MNRAS, 310, 1087

Somerville R. S., Primack J. R., Faber S. M., 2001, MNRAS, 320, 504

Somerville R. S., Hopkins P. F., Cox T. J., Robertson B. E., Hernquist L., 2008, MNRAS, 391, 481 (S08)

Srbinovsky J. A., Wyithe J. S. B., 2007, MNRAS, 374, 627

Srbinovsky J., Wyithe S., 2008, preprint (arXiv:0807.4782)

Stecker F. W., Malkan M. A., Scully S. T., 2006, ApJ, 648, 774

Stecker F. W., Malkan M. A., Scully S. T., 2007, ApJ, 658, 1392

Steidel C. C., Pettini M., Adelberger K. L., 2001, ApJ, 546, 665

Stengler-Larrea E. A. et al., 1995, ApJ, 444, 64

Telfer R. C., Zheng W., Kriss G. A., Davidsen A. F., 2002, ApJ, 565, 773

Tytler D., O'Meara J. M., Suzuki N., Kirkman D., Lubin D., Orin A., 2004, AJ, 128, 1058

Vanden Berk D. E. et al., 2001, AJ, 122, 549

Verma A., Lehnert M. D., Förster Schreiber N. M., Bremer M. N., Douglas L., 2007, MNRAS, 377, 1024

Williger G. M., Baldwin J. A., Carswell R. F., Cooke A. J., Hazard C., Irwin M. J., McMahon R. G., Storrie-Lombardi L. J., 1994, ApJ, 428, 574

Wright E. L., 2001, ApJ, 553, 538

Wright E. L., 2004, New Astron. Rev., 48, 465

Wright E. L., Reese E. D., 2000, ApJ, 545, 43

Wyder T. K. et al., 2005, ApJ, 619, L15

Xu C. K. et al., 2005, ApJ, 619, L11

Yüksel H., Kistler M. D., Beacom J. F., Hopkins A. M., 2008, ApJ, 683, L5

Zheng W. et al., 2004, ApJ, 605, 631

This paper has been typeset from a TeX/LaTeX file prepared by the author.